Metadislocation configurations and novel phason defects in the complex metallic alloy T-Al-Mn-Pd

L. Yang [a, b, *], M. Heggen [a], M. Feuerbacher [a, *], X. Han [b], R. E. Dunin-Borkowski [a]

[a] Ernst Ruska-Centre for Microscopy and Spectroscopy with Electrons, Forschungszentrum Jülich, 52428 Jülich, Germany

[b] Institute of Microstructure and Properties of Advanced Materials, Faculty of Materials and Manufacturing, Beijing University of Technology, Beijing 100124, China

∗ Corresponding authors: lu.yang@fz-juelich.de (L. Yang), m.feuerbacher@fz-juelich.de. (M. Feuerbacher)

Abstract

Metadislocations (MDs) are linear defects enabling plastic deformation in complex metallic alloys, a class of materials with large lattice parameters. We systematically investigate MD configurations in plastically deformed T-Al–Mn–Pd using aberration-corrected scanning transmission electron microscopy. Atomic-resolution imaging reveals that MDs in the T-phase can dissociate into energetically more favorable partials through a pure glide process. The analysis of MD dissociations allows for an estimate of the energy of the associated stacking faults. Adjacent MDs with opposite signs in the T-phase are found to interact and form dipolar configurations connected by shared chains of phason defects. We furthermore report on a new type of phason defect, which we identify as anti-phason. We discuss structural variants of anti-phasons, their role in the deformation- and MD-interaction processes and their energetical impact.

Keywords: Metadislocations; Complex metallic alloys; Scanning transmission electron microscopy; Defect interactions; Dislocation

1. Introduction

Complex metallic alloys (CMAs) are intermetallic compounds characterized by large lattice parameters and a correspondingly high number of atoms per unit cell, typically ranging between many tens and some thousands. CMA phases meanwhile have been identified in various alloy systems [1].

Because of the large lattice parameters, in CMAs conventional dislocation-based deformation mechanisms are prone to failure. Perfect dislocations are unfavorable to form since their large Burgers vectors would imply high elastic line energies. On the other hand, conventional partial-dislocation mechanisms are also unfavorable since high numbers of partials and potentially complex planar faults would be involved. In a number of CMAs this dilemma is resolved by a novel type of linear structural defect, the metadislocation (MD). MDs were discovered by Klein et al. in ε-phases in the system Al–Pd–Mn [2, 3], and later on found in other ε-type phases like Al–Pd–Fe [4] and Al–Ni–Rh [5]. MDs were further observed in orthorhombic $Al_{13}Co_4$ [6, 7] and orthorhombic T– phases in the Al–Mn–Pd system [8, 9]. The definition of MDs, which was initially limited to ε-phases, was generalized later on [9] in order to include related defects following the same structural principles in different materials. For an overview, see [10].

The core of an MD typically includes several hundreds of atoms per unit-cell thickness along its line direction [8]. As a result, any deformation process MDs are involved in is highly complex by itself. Even in the simplest case of MD glide in orthorhombic $Al_{13}Co_4$, a CMA with 102 atoms per unit cell [11, 12], a large number of coordinated atomic jumps along various crystallographic directions, summing up to a total jump distance of about 45 nm per glide step, takes place [7, 13, 14]. The glide mechanism of MDs in the Taylor phase in the system Al–Mn–Pd, referred to as T-Al-Mn-Pd, the material considered in the present paper, was firstly described in [8]. It was shown to involve movement of

the core plus a number of phasons, escorting the core. Phasons are particular linear defects in CMAs mediating local structural rearrangements [9, 15, 16]. Upon plastic deformation, the phason defects move ahead and locally transform the T-phase structure to allow for accommodation of the MD core. Glide of the MD leads to a local phase transformation in its wake that can be interpreted as the formation of a slab of R-Al-Mn-Pd, a structurally related phase in the alloy system [15, 17].

In two previous papers, we have described the MD types existing in T-Al-Pd-Mn and their properties [8, 9]. The present paper follows up, taking MD interactions, reactions and dissociations into account, in order to advance our understanding of the defects from merely structural aspects towards the deformation mechanism they are involved in. It is essential to investigate these aspects [18, 19] since the interactions of defects under applied stress play a critical role in the deformation, strain hardening, and failure mechanisms [18, 20], i.e. they essentially determine the plastic behavior of the material.

In the present study, we address the CMA phase T-Al-Mn-Pd, and systematically investigate interacting MD configurations in plastically deformed samples using atomic-resolution aberration-corrected scanning transmission electron microscopy (STEM). In T–Al–Mn–Pd, MDs with different Burgers vectors, associated with two, four, and six planar defects were identified [9]. The planar defects were observed to be either (100) slabs of R-phase, (001) phason planes, or inclined planar defects containing elements of both. Investigation of the configuration of MDs sharing phason defects or planar defects allows us to conclude on the nature of their interaction and their role in the plastic deformation process. Furthermore, we report on a novel defect of phason type, the anti-phason, and discuss its structural variants and functionality in the structure.

2. Experimental methods

A single crystal of the T–Al–Mn–Pd phase was grown employing the Bridgman technique, with a final composition of Al 75 at.%, Mn 21 at.%, and Pd 4 at.%. A cuboidal sample of approximately 1.5 mm × 1.5 mm× 4 mm was prepared and uniaxially deformed in compression using a modified Zwick Z 050 testing machine at 700 °C to a total strain of ~1.2 %. The compression direction was oriented perpendicular to the [010] direction and 45° inclined with respect to the [100] and [001] directions. This particular geometry leads to maximum shear stress for dislocation glide with [001] Burgers-vector direction on (100) planes. After deformation, the sample was rapidly unloaded and quenched to preserve its microstructural state. The dislocation density in the material was shown [9] to be higher than in an undeformed reference sample by three orders of magnitude, which demonstrates that the observed dislocation microstructure is a direct result of the deformation process.

The deformed T-Al-Mn-Pd sample was cut into slices and prepared for TEM investigations by subsequent grinding, dimpling, and argon-ion milling on a liquid nitrogen-cooled stage. Atomic-resolution STEM imaging was performed using an FEI Titan 80–200 [21] electron microscope with a Cs-probe corrector (CEOS GmbH) and a high-angle annular dark field (HAADF) detector. The microscope was operated at 200 kV. Z-contrast conditions were achieved using a probe semi-convergence angle of 24.7 mrad and an inner collection semi-angle of the detector of 88.4 mrad. The structural model was visualized using the VESTA software [22].

3. Structure model of T-Al-Mn-Pd

T-Al-Mn-Pd has an orthorhombic structure with lattice parameters a=1.47 nm, b=1.25 nm, c=1.26 nm, and 156 atoms per unit cell [23, 24]. Fig. 1 (a) shows a perspective view of the T- Al-Mn-Pd structure along the [010] direction based

on the atomic model developed by Klein et al. [15]. The complex structure can be represented in the form of an area-filling tiling in the (010) plane. As shown in Fig. 1 (a), the tiling for T-Al-Mn-Pd consists of elongated hexagons arranged in rows of alternating orientation, mutually tilted by 36° and displayed in white and yellow. The unit cell is indicated by a white cuboid, and a structure model is shown in the inset. One white or yellow hexagon tile represents 78 atoms per unit-cell thickness, equivalent to half the number of atoms in the unit cell.

Fig. 1 (b) shows a typical HAADF-STEM image of the T-Al-Mn-Pd structure. The Z-contrast imaging conditions emphasize atomic columns containing heavy atoms [25]. In T-Al-Mn-Pd, the atomic columns containing Pd atoms (Z = 46) are located at the centers, and those containing Mn atoms (Z = 25) at the vertices and edges of the hexagon tiles. The light Al atoms (Z = 13) do not lead to significant image contrast. Comparing Fig. 1 (a) and (b), we see that the contrast distribution in HAADF-STEM imaging corresponds well to the atomic structure model considering only the heavier atom columns.

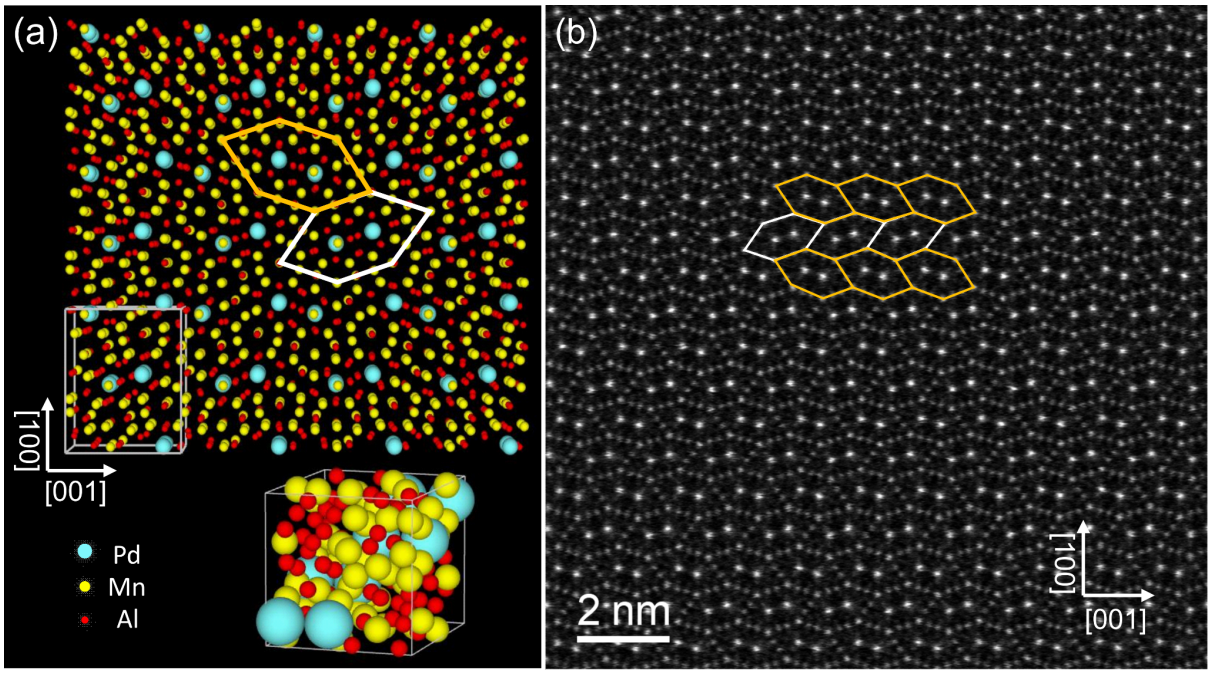

Fig.1. (a) Perspective view of the T-Al-Mn-Pd model along the [010] direction. The unit cell is indicated by a white cuboid. A space-filling model of the unit cell is shown in the inset. (b) High-resolution HAADF-STEM image of T–Al–Mn–Pd phase along the [010] direction. An area-filling tiling of elongated hexagons (white and yellow) is superposed.

4. Results and discussion

4.1 Metadislocation dissociation in T-Al-Mn-Pd

Fig.2 (a) shows a high-resolution HAADF-STEM image of a specimen region containing defects in plastically deformed T-Al-Mn-Pd. As described above, image regions of ideal T-phase structure, e.g. in the uppermost part, can be represented by a tiling of alternating hexagon rows. The lower part of the image contains regions consisting of rows of hexagon tiles in parallel orientation, indicating the presence of the R-phase. For example, in the lowermost part of the image, a slab of R-phase of ~4nm thickness along the [100] direction is shown with a superposed tiling of five parallel hexagon rows.

Since in the ideal T-phase, neighbored hexagon rows always appear in alternating orientations, the plane between two neighbored hexagon rows of equal orientation constitutes a (100) stacking fault (SF) in the T-phase. In this sense, any slab of R-phase can also be understood as a series of (100) SFs in the T-phase [8]. The slab indicated in Fig. 2 (a), accordingly, can be understood as a series of four SFs. In the center of Fig. 2 (a), two distinct linear defects are seen, separated by a distance of about 17.8 nm on a (100) plane. Fig. 2 (b) and (c) show magnified views of the left and right defect core, respectively, with superposed polygons marking their outlines. Fig. 3 displays a detailed tiling analysis of the region containing the MDs. In Fig. 3 (a), a hexagon tiling is superposed to the HAADF-STEM image, which clearly identifies the defects as MDs [9,10]. Additional green polygons represent the MD cores and red bow-tie-shaped tiles represent phason defects [15].

Phasons are linear defects specific to CMAs and quasicrystals, representing local tiling-sequence deviations that do not include a strain field [9, 15, 16]. In the T-phase, phason defects have [010] line direction and can be regarded as a

tiling element leading to an alteration of the stacking sequence [8, 9], which will be described in detail below.

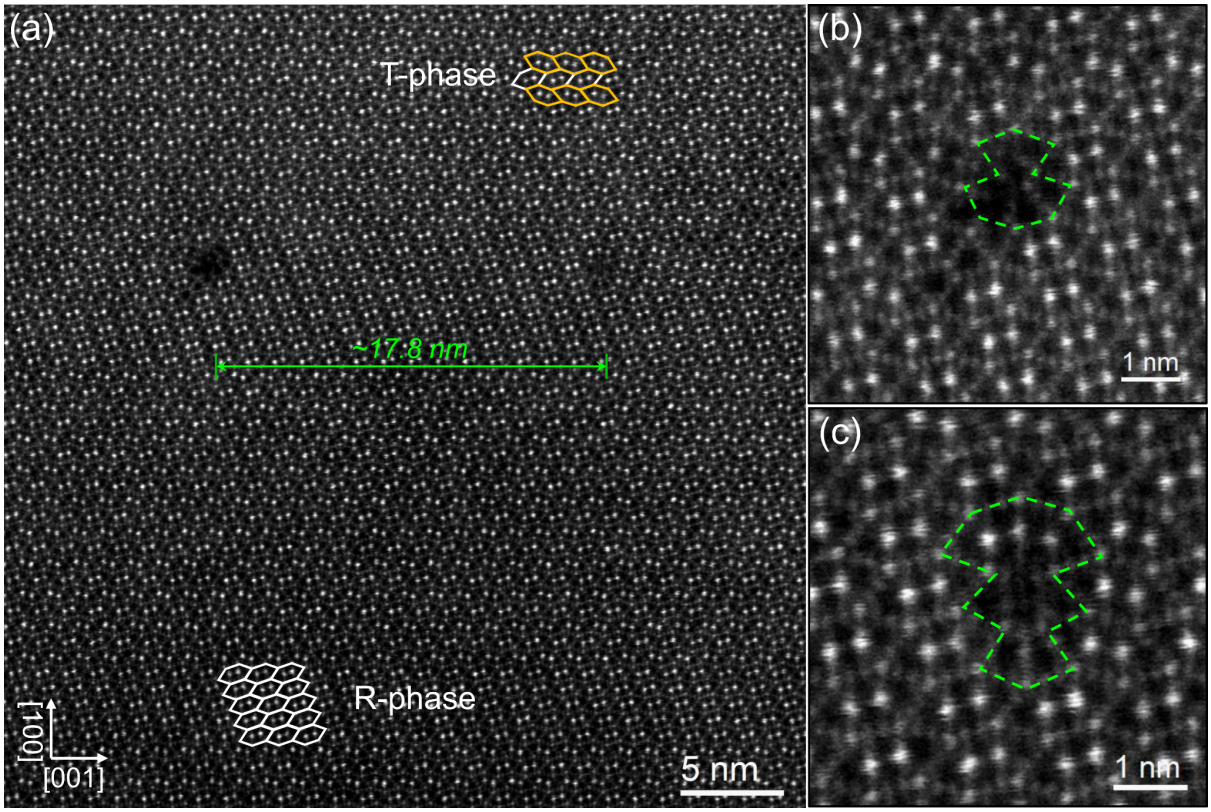

Fig. 2. (a) HAADF-STEM image showing two MDs on a (001) plane in plastically deformed T-Al-Mn-Pd. The distance between the two MD cores along the [001] direction is about 17.8 nm. The matrix structure is the T-phase represented by alternating rows of white and yellow hexagons. Slabs of the R-phase, represented by parallel rows of hexagons, are present in the lower region. (b) and (c): Magnified images of the MD left and right cores in (a), respectively, with green polygons as their tiling representations.

The tiling representation in Fig. 3 (a) reveals that the left MD is associated with four SFs, highlighted by parallel red dashed lines along [001] direction and labeled as No. 1-4. We will refer to an MD of this type as MD4 in the following. The right MD is associated with six SFs, four of which extend to the left (No. 1-4) and two to the right (No. 5 and 6), referred to as MD6 in the following. SFs No. 1-4 are formed by neighboring white, and SFs No. 5-6 SFs by neighboring yellow hexagon rows, respectively. The MD4 and MD6 are connected by four SFs No. 1-4, while SFs No. 5 and 6 extend away from the dislocations. One additional SF, marked by a pink dashed line, is passing through the image below

the MD4 and MD6. This SF is entirely independent of both MDs and can be disregarded. The lower of the two bow-tie-shaped phasons at the left side of MD4 displaces this SF along the [100] direction. For clarity, an equivalent tiling is depicted in Fig. 3 (b), in which the additional SF is not shown.

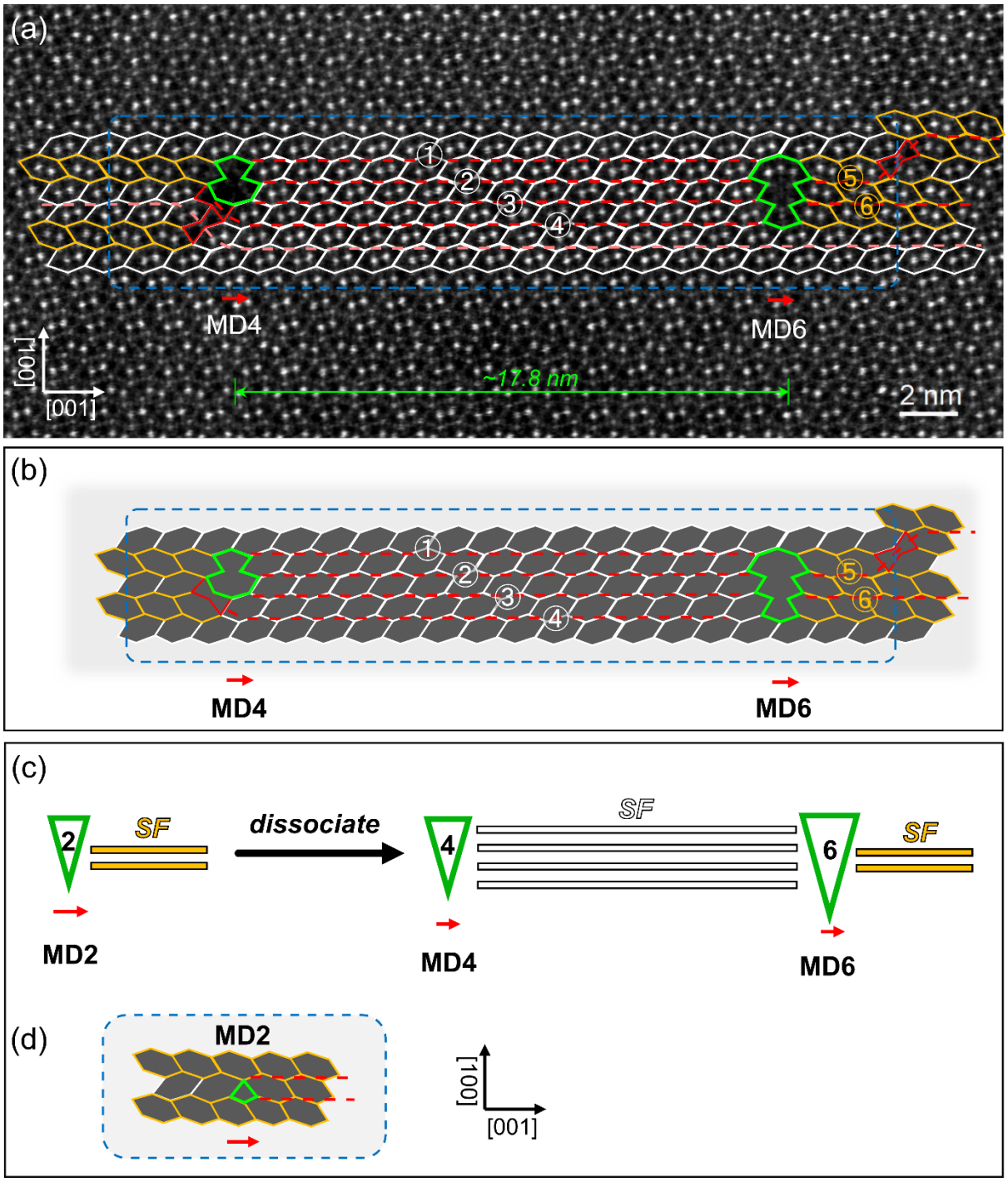

Fig. 3. (a) Tiling representation of the area containing the two MDs in Fig. 2(a). The green polygons and the red bow-tie-shaped tiles represent the MD cores and phason defects, respectively. The red dashed lines highlight SFs in the T-phase structure. The left-hand MD is

identified as an MD4, and the right-hand one is an MD6. Their Burgers vector directions are indicated by red arrows. (b) Equivalent tiling to (a) not including the additional SF passing below the MD cores (pink dashed line in (a)). (c) Schematic of the dissociation process of an MD2 into an MD4 and an MD6 separated by SFs. (d) Tiling of an MD2 corresponding to the schematic drawing in (c). A red arrow indicates its Burgers vector direction.

In order to determine the Burgers vectors of an MD, a closed circuit can be constructed along the polygon edges of its core [10]. This circuit is then transferred to an unstrained structure described by perfect hexagon tiles. The resulting closure failure corresponds to the Burgers vector of the MD. Following this procedure, the Burgers vector of the MD4 in Fig. 3 (a) is identified as $\vec{b}_4 = \frac{c}{\tau^3}(001)$, where τ is the number of the golden mean, corresponding to a Burgers vector magnitude of 0.297 nm. The Burgers vector of the MD6 in Fig. 3 (a) yields $\vec{b}_6 = \frac{c}{\tau^4}(001)$, with a magnitude of 0.184 nm. It has previously been demonstrated that the Burgers vector of this type of MD has no component along the [010] viewing direction [9]. The two Burgers vectors are oriented in the same direction on the (100) plane, as indicated by the red arrows in Fig. 3 (a). The net Burgers vector of the MD4 and the MD6 in Fig. 3 (a) thus yields $\vec{b}_4 + \vec{b}_6 = \frac{c}{\tau^3}(001) + \frac{c}{\tau^4}(001) = \frac{c}{\tau^2}(001)$, with a magnitude (0.297 + 0.184) nm = 0.481 nm. This net value corresponds to the Burgers vector of an MD associated with two SFs (MD2). We can hence interpret the total configuration as a dissociation of an MD2 into an MD4 and an MD6 on the (100) plane. This is perfectly consistent with the observation that the net effect of the configuration is the extension of two SFs away into the matrix.

Fig. 3 (c) diagrammatically summarizes this MD2 dissociation using the scheme described in Supplementary Fig. S1. The MD cores are depicted as green triangles with their Burgers vector directions indicated by red arrows. The two types of SF associated with the MDs, consisting of neighboring white and yellow hexagon rows, are depicted by white and yellow bars. Fig. 3 (d) displays the tiling

representation of the undissociated MD2, with its two SFs both extending into the matrix on the right side of its core.

Fig. 4 (a) shows another specimen region containing an MD4 and an MD6 and the corresponding tiling representation. In contrast to the configuration of Fig. 3, here the MD4 and an MD6 are connected by two SFs, and the distance between their cores is ~32.9 nm. Again, the Burgers vectors of the MD4 and MD6 have the same direction (red arrows). The Burgers-circuit analysis reveals that their net Burgers vector also is 0.481nm, indicating that the microstructure in Fig. 4 (a) results from an MD2 dissociation diagrammatically displayed in Fig. 4 (a). Clearly, the MD6 and MD4, connected by two SFs(yellow bars), have four and two associated SFs (white bars) on their respective left and right side. The corresponding tiling representation of the MD2 structure with two additional SFs passing the MD at the top is depicted in Fig. 4 (c).

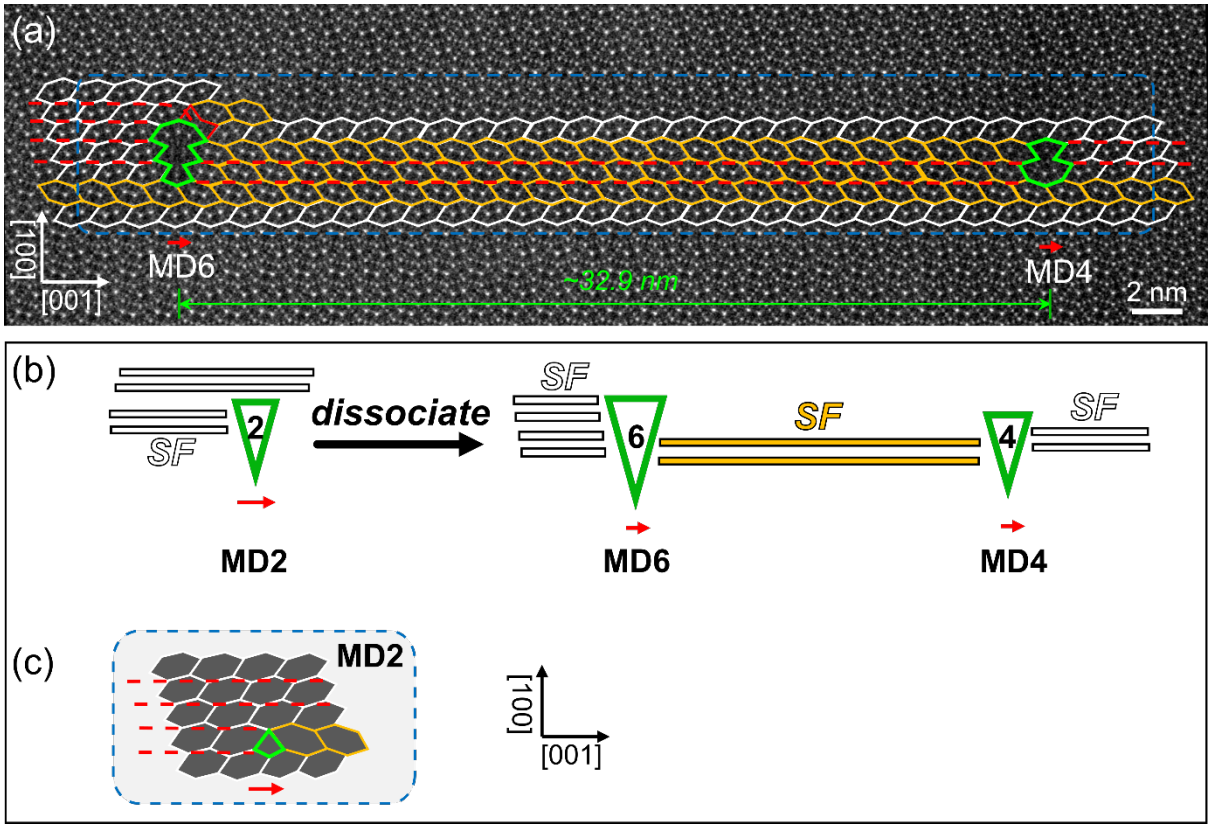

Fig. 4. (a) HAADF-STEM image and corresponding tiling displaying an MD4 and an MD6 with a core distance of about 32.9 nm. Their Burgers vectors are indicated by red arrows. The red dashed lines highlight SFs in the T-phase structure. (b) Schematic drawing summarizing

the process of an MD2 dissociation into an MD4 and an MD6. (c) Tiling of an MD2 with two additional SFs.

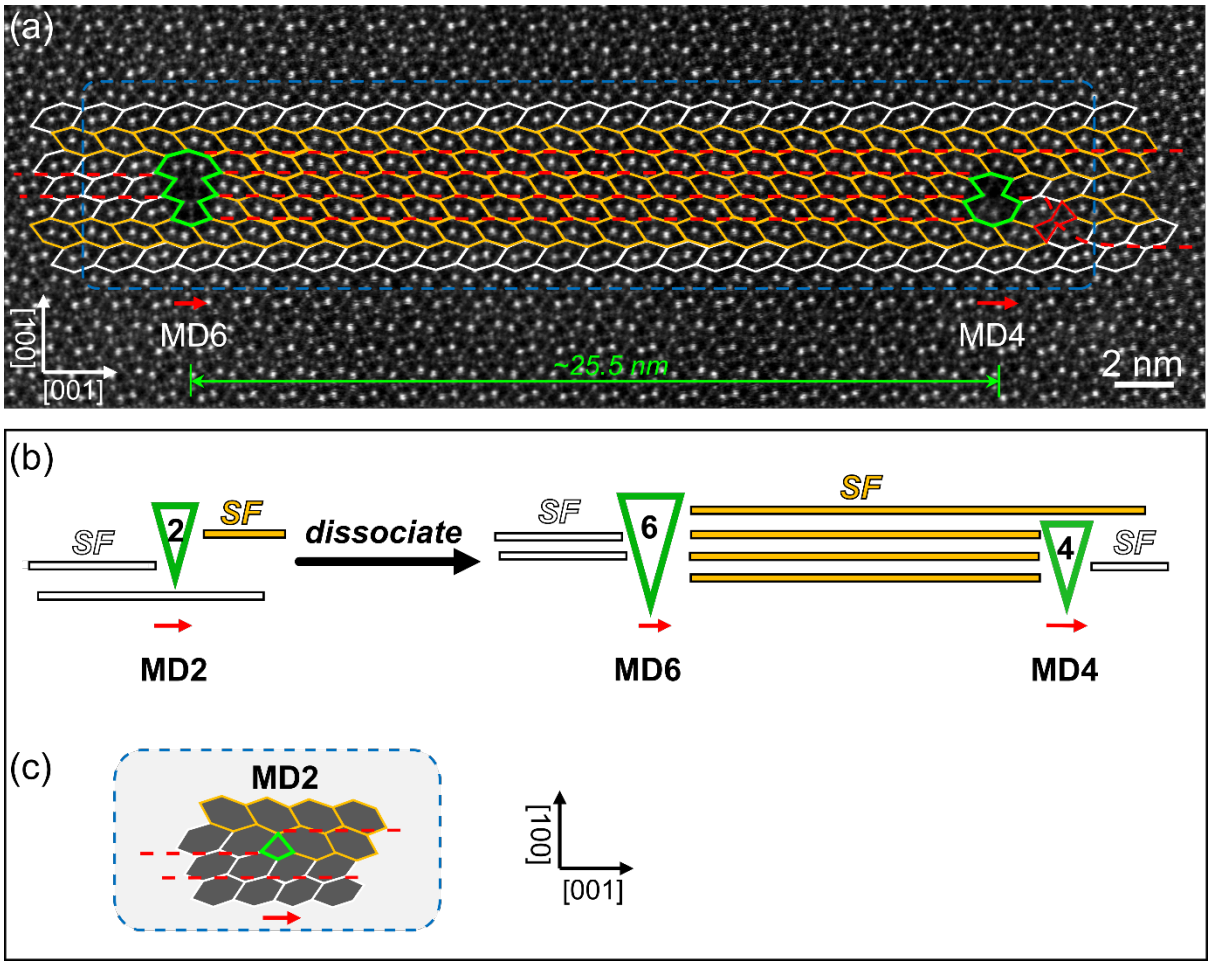

Fig. 5. (a) HAADF-STEM image and corresponding tiling revealing a microstructural situation containing an MD4 and an MD6 along [001] direction, the distance between their cores (green polygons) is about 25.5 nm. Their Burgers vectors are indicated by red arrows. The red dashed lines highlight SFs in the T-phase structure. (b) Schematic drawing summarizing the process of an MD2 dissociation into an MD4 and an MD6. (b) The tiling of the MD2 structure corresponds to the schematic drawing in (c).

Fig. 5 (a) shows another different configuration of an MD4 and an MD6 and its corresponding tiling representation. The net Burgers vector yields (0.297 + 0.184)nm= 0.481nm, indicating that the configuration in Fig. 5 (a) again can be understood as an MD2 dissociation.

As shown in Fig. 5 (a), on the right side of the MD4 core, one associated SF is redirected by a phason defect. On the left and right sides of the MD6 core, there are two and four associated SFs, respectively. The MD4 and the MD6 share

three SFs in their intermediate region, and the distance between their cores is ~ 22.5 nm. Note that there is one SF on the right side of MD6, passing above the core of MD4, which is not associated with the MD4 core. The corresponding MD2 dissociation is schematically displayed in Fig. 5 (b). It can be seen that the whole MD4 + MD6 structure is associated with two SFs (white bars) on the left and two SFs (one yellow bar on top and a white bar below) on the right. Accordingly, the equivalent configuration is an MD2 (Fig. 5 (c)) associated with one SF on the left and right side, respectively (white and yellow bar) and one additional SF passing the MD2 at the bottom (white bar). To sum up, the microstructural configurations analyzed in Figs. 3-5 correspond to three different dissociations of an MD2 into an MD4 and MD6.

The elastic energy of an MD can be approximated as $E \approx \mu \cdot |\vec{b}|^2$, where μ is the shear modulus [26, 27]. Inserting the values for the respective Burgers vectors, the total elastic strain energy of MD4 and MD6 is calculated as $E4 + E6 = \mu \cdot |\vec{b}_4|^2 + \mu \cdot |\vec{b}_6|^2 = 0.122\mu$. This is almost half the value of an undissociated MD2, for which $E2 = \mu \cdot |\vec{b}_2|^2 = 0.231\mu$.

On the other hand, the MD2 dissociation requires creating additional SFs between the MD4 and MD6 cores, which correspondingly introduces additional fault-plane energy into the ideal T-phase. According to Frank's criterion [28], MD2 dissociation will take place if the total energy balance is favorable, i.e. if the decrease in elastic energy upon dissociation is higher than the energy increase caused by the additional SFs.

The MD2 dissociation into MD4 and MD6 leads to a reduction of local elastic energy of $E' = E2 - (E4 + E6) = 0.109\mu$, which must be higher than the value of energy increase caused by the two additional SFs that connect the two MD cores. In order to obtain an estimate of the upper limit for the SF energy (SFE), we make the (certainly questionable) assumption that the configurations in Figs. 3 - 5 represent equilibrium situations. For the MD2 dissociation in Fig.

3 (a), the MD4 and MD6 are connected by four SFs. The dissociation length L, the distance between the MD4 and MD6 cores, amounts to 17.8 nm. Assuming a μ value of 30 GPa [26, 27], the upper limit value of the SFE can be estimated as $E'/(2 * L) \approx 0.092\,J/m^2$. Analogously, for the case in Fig. 5 (a) with a dissociation length of ~25.5 nm we obtain a value of $E'/(2 * L) \approx 0.064\,J/m^2$. We thus obtain an average of 0.078 J/m^2 as upper limit for the SFE of in T-Al-Pd-Mn. Note that due to the probably violated assumption of equilibrium, these values can at best be considered order-of-magnitude estimates. However, the value is comparable and of the same order of magnitude as typical experimental and theoretical SFE values reported in simple metals, for instance, copper (~ 0.04 J/m^2) and aluminum (~ 0.2 J/m^2), and alloys e.g. Ti-Al (0.082-0.31 J/m^2) [29-31]. Note furthermore, that the MD2 dissociation in Fig. 4 (a) cannot be evaluated in this fashion, as the dissociation does not change the number of SFs between the MDs.

It is known that plastic deformation in the T-phase is mediated by MDs moving by pure glide on (1 0 0) planes [8, 9]. The MDs shown in Figs. 3-5 are all associated with (100) SFs and their Burgers vectors are parallel to their direction of motion, i.e., they move by pure glide. Accordingly, the MD2 dissociation reactions described above are pure glide dissociations on (100) planes in the T-phase matrix. This process is basically comparable to the well-known formation of extended dislocations e.g. in fcc metals, where perfect dislocations dissociate into Shockley partials enclosing an SF [28]. Note, however, that there also is a principal difference: while in fcc metals the dissociation starts with a perfect dislocation, the present process involves a partial dislocation dissociating into even smaller partials.

The compression direction of the deformation experiments was oriented perpendicular to the [010] direction and inclined by 45° with respect to the [100] and [001] directions. Hence, the maximum shear stress is resolved on (100) planes and indeed favors glide of MDs having [001] Burgers vectors and their

dissociation on this plane. By contrast, MD dissociation by pure climb was previously observed in the T–Al–Mn–Fe system [9]: by climbing along the [100] direction, an MD2 with two associated phason planes was found to dissociate into an MD6 and an MD4 with six and four phason planes, respectively. Moreover, the formation of MDs in orthorhombic ε-phases of the system Al–Pd–Mn is necessarily associated with a set of phason planes. In these materials, MDs move by pure climb and dissociate with shared phason planes [32, 33].

In the present study, besides the pure glide dissociations, we also observed an MD configuration involving mixed glide and climb (see Supplementary Fig. S2).

4.2. Metadislocation dipoles in T-Al-Mn-Pd: Interactions of MD6s

Fig. 6 (a) shows a high-resolution HAADF-STEM image of a specimen region containing two interacting MD6s on parallel (100) glide planes in the deformed T-Al-Mn-Pd. Fig. 6 (b) shows the corresponding tiling. The two core tiles of MD6s (green polygons) have opposite orientations and their Burgers vectors have opposite directions, as indicated by red arrows. The two MD6s are mutually connected via two shared chains of phason and while four SFs extend into the matrix on their left and right. The distances between the two MD6 cores along [100] and [001] directions are both ~5.2 nm, i.e. the two MD6s form an MD dipole in a 45-degree configuration. However, MD6 dipole configurations with smaller and greater angles are also possible, as shown in Figs. 6 (c) and (d).

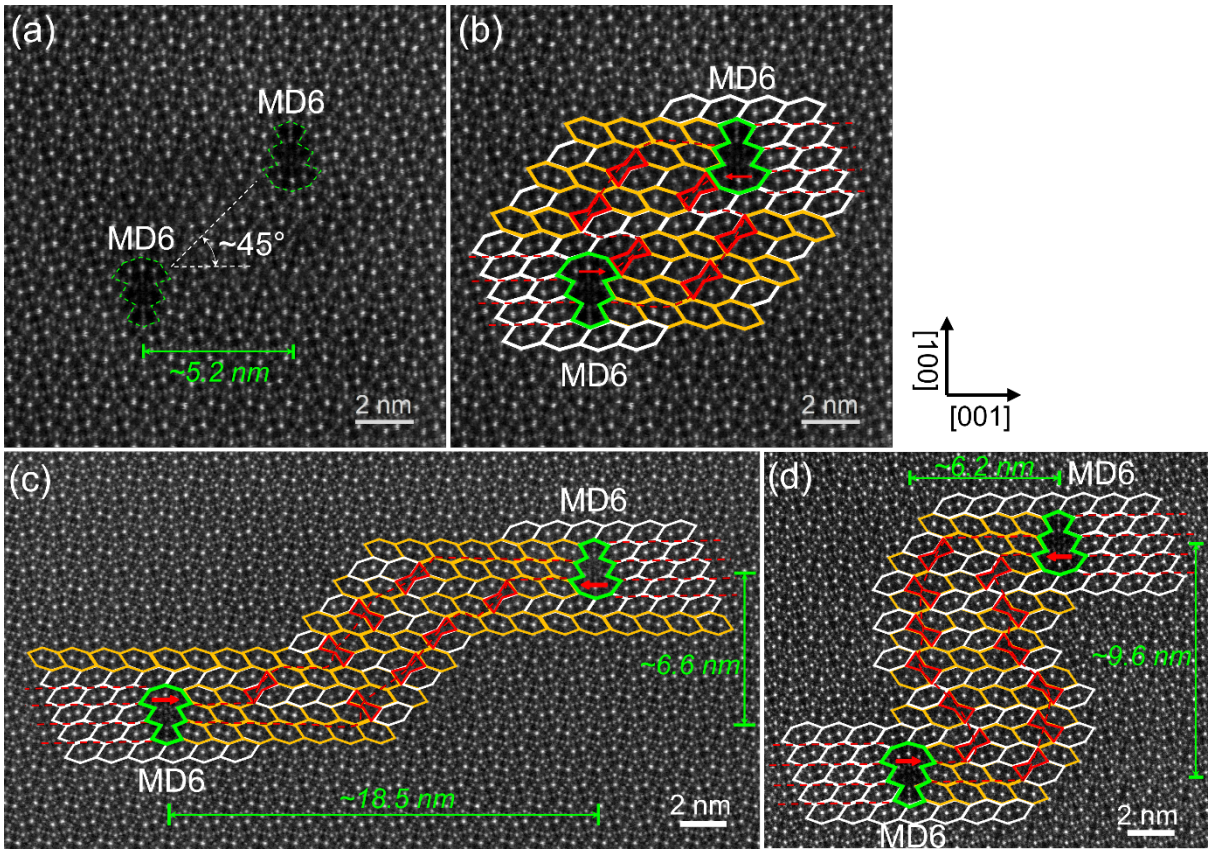

Fig. 6. HAADF-STEM images and corresponding tilings revealing microstructural configurations of interacting MD6s. The MD6 cores (green polygons) are connected by two chains of phason defects. Their Burgers vectors are indicated by red arrows.

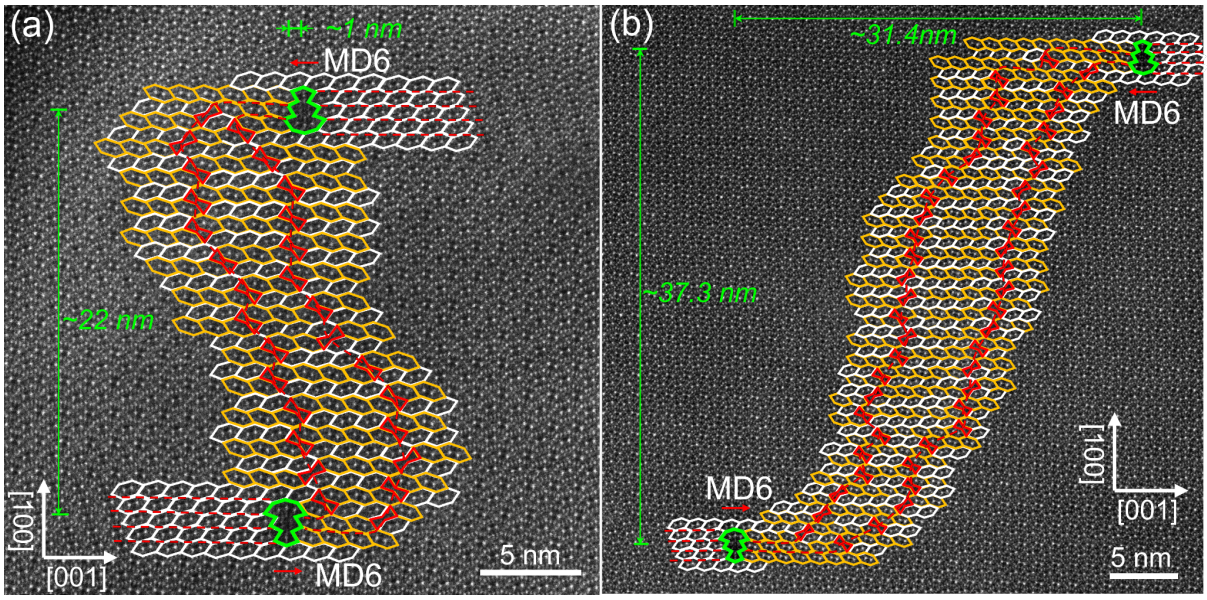

Fig. 7. HAADF-STEM images and corresponding tilings revealing interacting MD6s with long distances between the (100) glide planes: (a)~22nm, (b) ~37.3 nm. The MD6 cores (green polygons) are connected by two chains of phason defects. Their Burgers vectors are indicated by red arrows.

In simple crystals, edge dislocations of opposite sign gliding on parallel planes tend to form stable dislocation dipoles in a 45-degree configuration [18, 28], which is similar to the configuration in Fig. 6 (a). However, it should be noted that dislocations in simple crystals interact purely via the stress field, while the MD interactions shown here involve phason defects. Fig. 7 (a) and (b) demonstrate that MD6s with a distance between the (100) glide planes as far as 20-40 nm can still interact by sharing long chains of phasons in the T-phase matrix. Furthermore, we observed MD6 dipole configurations sharing two [001] SFs, constituting a thin slab of R-phase terminated by two MD6 cores in the T-phase matrix. Fig. 8 (a) shows such a configuration with a distance between the two cores of about 16.1 nm. Due to the opposite Burger vectors of the MDs, it should be unstable, but the fact that it nevertheless can be observed may be taken as an indication that in such configurations the dislocation mobility is rather low. Fig. 8 (b) exhibits an MD dipole configuration similar to Fig. 8 (a) but including a [100] lattice offset by one lattice parameter.

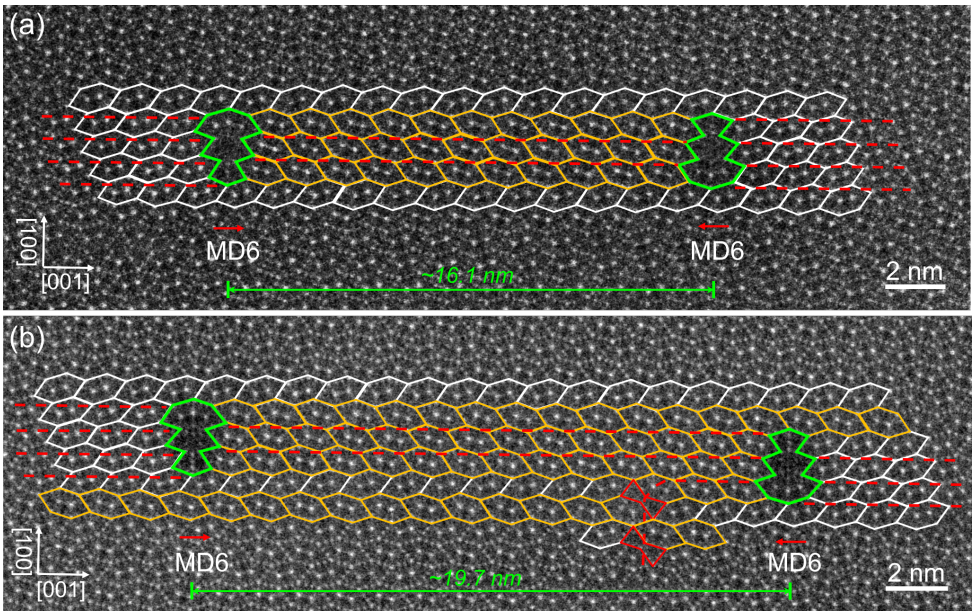

Fig. 8. HAADF-STEM images and corresponding tilings revealing two microstructural configurations of two interacting MD6s: (a) two MD6 cores (green polygons) are mutually connected by two SFs along the [001] direction at a distance of about 16.1 nm. Their Burgers vectors are indicated by red arrows and have opposite directions. (b) a configuration similar

to (a) but has a [100] lattice offset between the two MD6 cores. The distance between the cores is about 19.7 nm.

4.3. A new type of phason defect in T-Al- Mn-Pd: Anti-phason

Phason defects play a critical role in the deformation mechanism of T-Al-Mn-Pd [8, 9]. They are required to accommodate MDs in the ideal T-phase structure, move along with the MDs as escort defects upon plastic deformation, and, as shown above, also mediate MD interactions.

Fig. 9 shows a new type of zigzag-shaped defect and the corresponding tiling representation. This zigzag-shaped defect (red polygon) has an extension of three hexagon tiles along the [100] direction and simultaneously displaces two white SFs by one lattice constant along the [100] direction. The course of the SFs is marked by red dashed lines. The novel defect thus takes on a similar function as the known phason defects. As depicted in the inset Fig. 9 (c), using vectors of a regular pentagon a1 to a5, a circuit created around the defect shows no closure failure, evidencing that it does not possess a strain field, i.e. it is not a dislocation. We can thus conclude that the zigzag-shaped defect in Fig. 9 (a) is a novel defect with all characteristic features of a phason defect in the T-phase.

Fig. 10 (a) shows a HAADF-STEM micrograph involving four zigzag-shaped phasons in succession (indicated with red dotted polygons), which together constitute a (101) planar defect. The tiling in Fig. 10 (b) clearly shows the principal function of these defects in structural rearrangement: Adding one zigzag-shaped defect increases the displacement of two SFs by one lattice constant, and four defects lead to a total displacement of four lattice constants along the [100] direction.

Fig. 10 (c) shows another situation involving multiple zigzag-shaped defects, which rearrange the local course of two SFs. Differently, except for three zigzag-shaped phasons, a shorter defect is present in the upper right side of Fig. 10 (c). The shorter defect is structurally close to the zigzag-shaped phason but

has a smaller extension along the [100] direction. Compared to the zigzag-shaped phasons, this shorter defect displaces one white SF by only one lattice constant. In the inset of Fig. 10 (d), a circuit created around the shorter defect confirms that it is not associated with a strain field. Therefore, this shorter defect is also a type of phason and structurally can be regarded as the basic unit of the novel phason type.

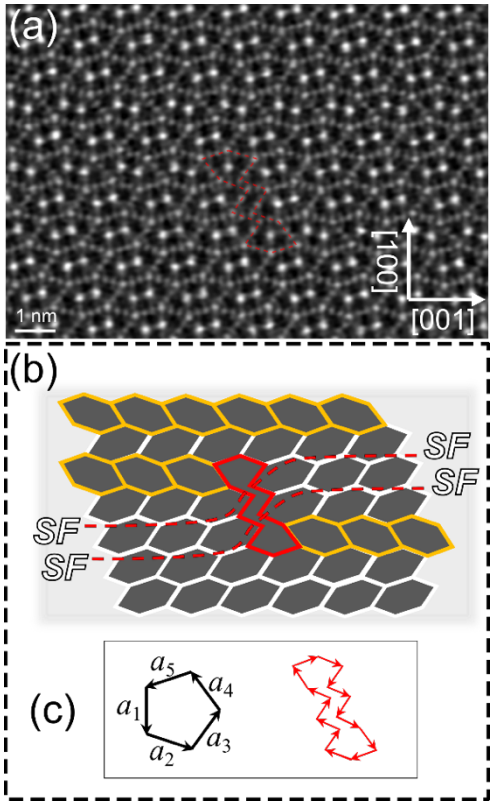

Fig. 9. (a) HAADF-STEM micrograph containing a novel type of zigzag-shaped defect in the T-phase matrix. (b) Corresponding tiling representation showing the defect (red polygon) and associated stacking faults. (c) Analysis of the Burgers circuit of this defect in terms of vectors of a regular pentagon, confirming that it does not introduce a strain field.

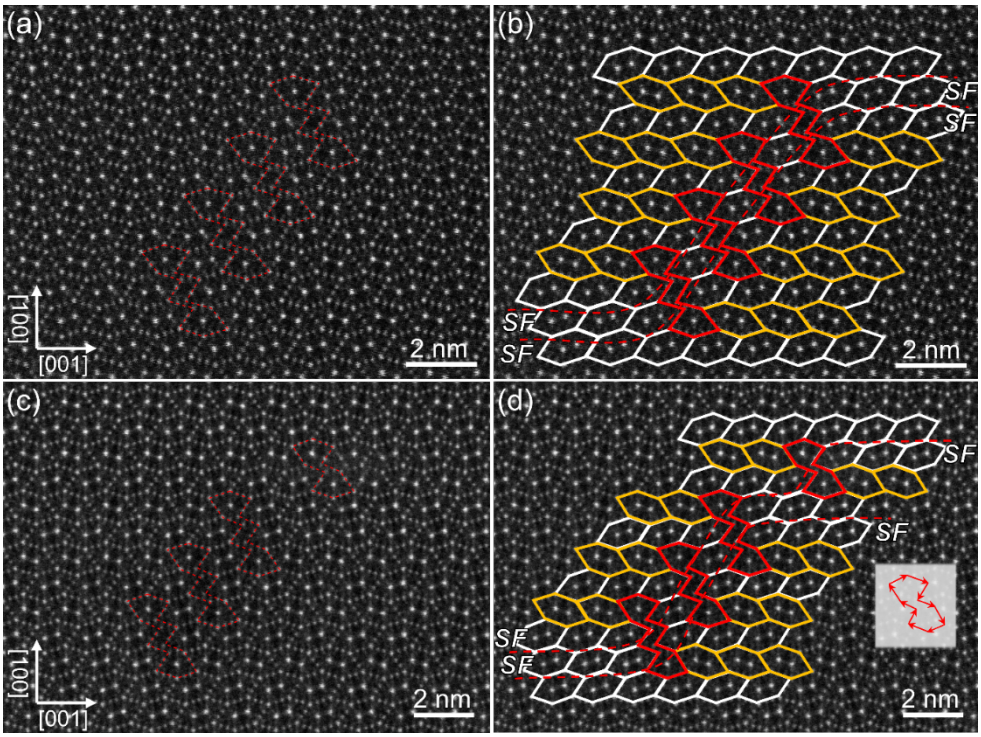

Fig. 10. (a) HAADF-STEM micrograph showing continuous four phason defects (the same type in Fig. 10), and (b) corresponding tiling representation. (c) HAADF-STEM micrograph showing continuous three phason defects and another shorter defect, and (d) corresponding tiling representation. The inset of (d) analyzes the Burgers circuit of the shorter defect in terms of vectors of a regular pentagon, confirming that it is also a phason defect in the T-phason.

We thus see that the action of the known phason defect, represented in a tiling by a bow-tie-shaped tile, is counteracted by the novel type of phason. Tilings altered by bow-tie-shaped phasons are locally re-established by zigzag-shaped phasons (see Supplementary Fig. S3). In other words, the previously known and the novel type of phason defect act complementarily in the lattice and hence can mutually annihilate. Therefore, we will in the following refer to the novel type of phason defect as “anti-phason”. As schematically depicted in Fig. 11 (a), a conventional phason (Ph+) can complete a phason dipole with an anti-phason (Ph-).

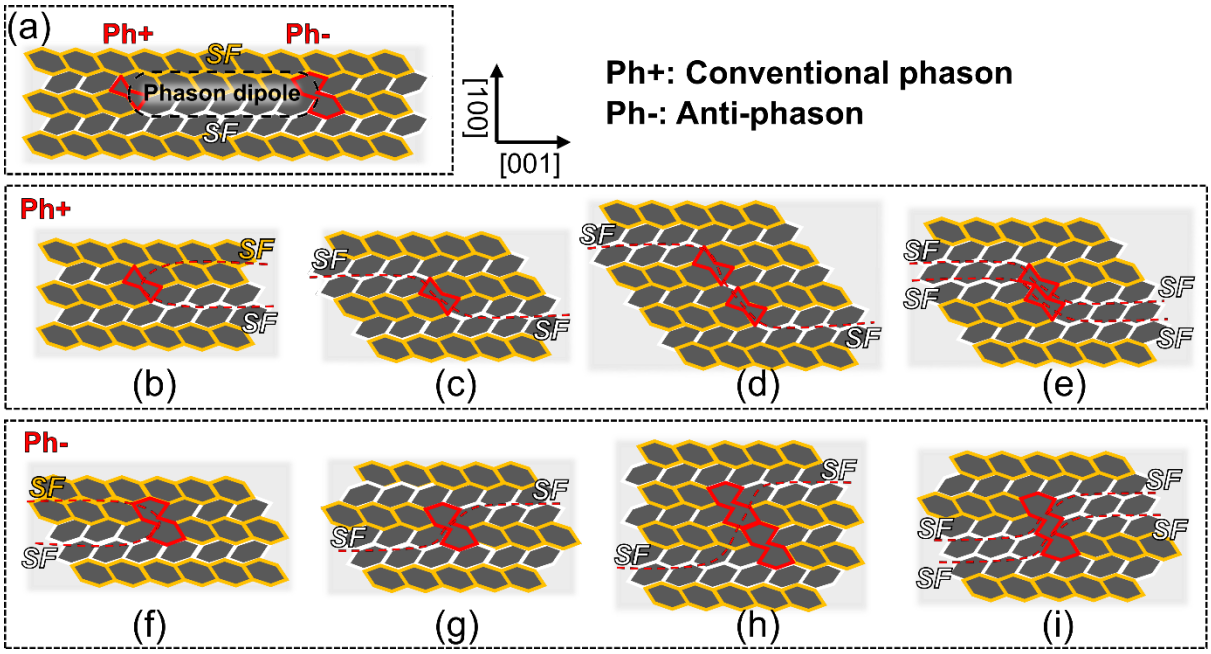

Fig. 11. (a) Schematic tiling representation of a phason dipole, constituted by a conventional phason (+Ph) and an anti-phason (-Ph). (b-e) and (f-i) Tiling representations of various structural situations based on conventional phasons and anti-phasons indicate their roles in stacking-fault displacement in the T-phase matrix.

Figs. 11 (b-e) display typical tilings involving conventional phasons in the T-phase matrix, which have been discussed in [9]. Correspondingly, Figs. 11 (f-i) display the analogous structural situations for the anti-phasons.

In Fig. 11 (f), one anti-phason redirects one SF as indicated by the red dotted line. Figs. 11 (g) and 11 (h) represent structural situations involving one and two anti-phasons, which lead to SF displacements by one and two lattice constants along [100], respectively. The zigzag-shaped defect in Fig. 11 (i) is a variant of the basic anti-phason and induces the displacement of two neighboring SFs by one lattice constant. This situation corresponds to the experimentally observed microstructure shown in Fig. 9 (a) and Fig. 10 (a). Meanwhile, the microstructure in Fig. 10 (c) can be understood as a combined result of the situations in Fig. 11 (g) and Fig. 11 (i).

It should be pointed out that the anti-phasons were experimentally not observed previously, while the conventional bow-tie-shaped phasons are abundantly present in deformed T-phase CMAs [8, 9]. This asymmetry in

experimental observation frequency may be related structural and energetical disparities between conventional phasons and anti-phasons. First, while the conventional phason is represented by a simple bow-tie-shaped hexagon, the anti-phason unit involves a decagon of a more complex shape. The anti-phason involves a bigger volume and the structural rearrangement of more atoms and may introduce more complex local interfaces. Based on a potentially higher structural complexity, it seems reasonable to infer that the formation of anti-phasons is structurally less favorable and thus energetically more costly compared to the conventional phasons, which may explain the asymmetry in the frequency of experimental observation between conventional phasons and anti-phasons.

In this light, let us revisit some of the local configurations experimentally observed: Fig. 5 shows the occurrence of two differently directed SFs at the right-hand side of the MD4. These SFs could mutually annihilate each other, leading to a energetically more favorable situation. However, this would require the involvement of an anti-phason, which due to its higher energetic cost represents an energy barrier for the annihilation process would be required (see Fig. 11 (a) for comparison).

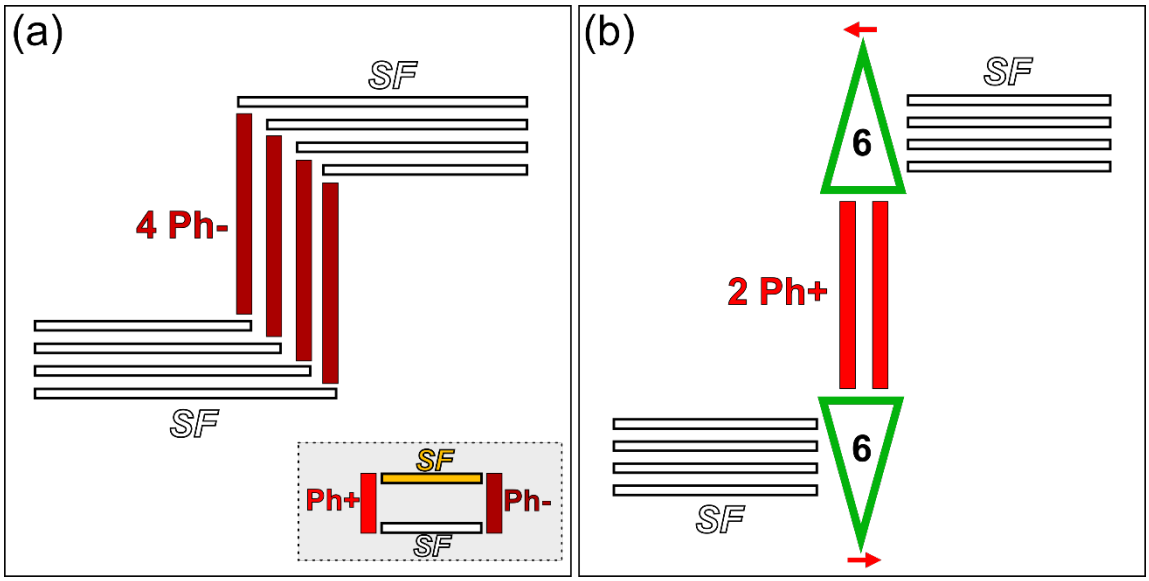

Fig.12. (a) Schematic indicating four SFs are connected by four chains of anti-phason (4 Ph-). For clarity, the inset displays a schematic drawing corresponding to the tiling of the phason dipole in Fig. 11 (a). (b) Schematic indicating the configuration that two MD6s with opposite Burgers vector directions are connected by two chains of phasons (2 Ph+), corresponding to the observations in Figs. 6 and 7.

The formation of MD6 dipoles as shown in Figs. 6 and 7 can be understood assuming that anti-phasons are energetically more costly, as well. Consider a series of four SFs, e.g. created by movement a single MD4 moving through the structure. Now if the MD4 climbs upwards by a few lattice constants for whatever reason, the upper and lower parts of the SF segments have to be connected by four chains of anti-phasons (dark red bars), as schematically shown in Fig. 12 (a). The starting situation of four chains of anti-phasons (4 Ph-) in Fig. 12 (a) can be replaced by two MD6s with opposite Burgers vector direction, connected by two chains of conventional phasons (bright red bars, 2 Ph+), as shown in Fig. 12 (b). If four chains of anti-phasons are indeed energetically more expensive than two chains of phasons plus two MD6, this would lead to a configuration of lower total energy and correspond to the observations in Figs. 6 and 7.

In this sense, the formation of the configuration observed in Figs. 6 and 7 might be explained by climb of a MD4, creating a MD6 dipole in its wake to prevent the formation of a potentially energetically unfavorable chain of phason elements. Similarly, the initial configuration can also be created by two MD4 with opposite Burgers vectors, moving on planes separated by a few lattice constants and annihilating by climb.

5. Conclusions

In the current work, we present atomic-scale observations of various MD configurations in a plastically deformed T-Al–Mn–Pd complex metallic alloy using HAADF-STEM imaging and provide a detailed structural analysis. It is

demonstrated that MD2s can dissociate into an MD4 and an MD6 by pure glide on (100) planes in the T-phase leading to the introduction of SFs between the MD4 and MD6 cores and a decrease of total elastic energy. Assuming that the observed configurations are in equilibrium, we estimate the corresponding SFE as 0.078 J/m^2. The interactions of MD6s and related configurations are studied, revealing that two MD6s with opposite signs gliding on parallel (100) planes can form MD dipoles in variable configurations, connected mainly by shared chains of phason defects. In addition, we find a new type of phason defect, the so-called anti-phason. It is suggested that anti-phasons are energetically more costly than conventional phasons and could be related to the formation of MD6 dipoles. Structural variants of anti-phason and corresponding functions in the lattice are systematically discussed.

Acknowledgments

We thank C. Thomas and M. Schmidt for producing the sample material. L. Yang thanks P.F. Cao, P.Y. Tang, H.C. Du, and L. Jin for the STEM experiments and valuable discussions. We thank support by the Deutsche Forschungsgemeinschaft (PAK 36) and the Helmholtz-OCPC Postdoc-Program from the Helmholtz Association and the Office of China Postdoc Council (grant ZD2019018). L. Yang and X. Han thank support by the Basic Science Center Program for Multiphase Evolution in Hypergravity of the National Natural Science Foundation of China (grant 51988101), the Natural Science Foundation of China (grant 91860202), and the “111” project (grant DB18015).

References

[1] K. Urban, M. Feuerbacher, Structurally complex alloy phases, Journal of non-crystalline solids 334 (2004) 143-150.
[2] H. Klein, M. Feuerbacher, Structure of dislocations and stacking faults in the complex intermetallic ξ’-(Al–Pd–Mn) phase, Philosophical Magazine 83(36) (2003) 4103-4122.
[3] H. Klein, M. Feuerbacher, P. Schall, K. Urban, Novel type of dislocation in an Al-Pd-Mn quasicrystal approximant, Physical review letters 82(17) (1999) 3468.

[4] M. Feuerbacher, S. Balanetskyy, M. Heggen, Novel metadislocation variants in orthorhombic Al–Pd–Fe, Acta Materialia 56(8) (2008) 1849-1856.
[5] W. Sun, Y. Chen, Z. Zhang, Defect-modulated structures in Al–Ni–Rh crystalline approximants, Philosophical Magazine 87(18-21) (2007) 2815-2822.
[6] M. Heggen, D. Deng, M. Feuerbacher, Plastic deformation properties of the orthorhombic complex metallic alloy phase Al13Co4, Intermetallics 15(11) (2007) 1425-1431.
[7] M. Heggen, L. Houben, M. Feuerbacher, Metadislocations in the structurally complex orthorhombic alloy Al13Co4, Philosophical Magazine 88(13-15) (2008) 2333-2338.
[8] M. Heggen, L. Houben, M. Feuerbacher, Plastic-deformation mechanism in complex solids, Nature materials 9(4) (2010) 332-336.
[9] M. Heggen, L. Houben, M. Feuerbacher, Metadislocations in the complex metallic alloys T–Al–Mn– (Pd, Fe), Acta Materialia 59(11) (2011) 4458-4466.
[10] M. Feuerbacher, M. Heggen, Metadislocations, Dislocations in solids 16 (2010) 109-170.
[11] J. Grin, U. Burkhardt, M. Ellner, K. Peters, Crystal structure of orthorhombic Co4Al13, Journal of Alloys and Compounds 206(2) (1994) 243-247.
[12] T. Gödecke, M. Eliner, Phase Equilibria in the Aluminium-rich Portion of the Binary System Co-Al and in the Cobalt/Aluminium-rich Portion of the Ternary System Co-Ni-Al / Phasengleichgewichte im aluminiumreichen Teil des binären Systems Co-Al und im kobalt-aluminiumreichen Teil des ternären Systems Co-Ni-Al, International Journal of Materials Research 87(11) (1996) 854-864.
[13] M. Heggen, M. Feuerbacher, Core structure and motion of metadislocations in the orthorhombic structurally complex alloy Al13Co4, Materials Research Letters 2(3) (2014) 146-151.
[14] M. Heidelmann, M. Heggen, C. Dwyer, M. Feuerbacher, Comprehensive model of metadislocation movement in Al13Co4, Scripta materialia 98 (2015) 24-27.
[15] H. Klein, M. Boudard, M. Audier, M. De Boissieu, H. Vincent, L. Beraha, M. Duneau, The T-Al3 (Mn, Pd) quasicrystalline approximant: chemical order and phason defects, Philosophical magazine letters 75(4) (1997) 197-208.
[16] L. Beraha, M. Duneau, H. Klein, M. Audier, Phason defects in Al-Pd-Mn approximant phases: another example, Philosophical Magazine A 78(2) (1998) 345-372.
[17] K. Robinson, The determination of the crystal structure of Ni4Mn11Al60, Acta Crystallographica 7(6-7) (1954) 494-497.
[18] J.P. Hirth, J. Lothe, Theory of Dislocations, Wiley1982.
[19] V.A. Lubarda, J. Blume, A. Needleman, An analysis of equilibrium dislocation distributions, Acta metallurgica et materialia 41(2) (1993) 625-642.
[20] U. Messerschmidt, Dislocation dynamics during plastic deformation, Springer Science & Business Media2010.
[21] A. Kovács, R. Schierholz, K. Tillmann, FEI Titan G2 80-200 CREWLEY, Journal of large-scale research facilities JLSRF 2 (2016) 43.
[22] K. Momma, F. Izumi, VESTA 3 for three-dimensional visualization of crystal, volumetric and morphology data, Journal of applied crystallography 44(6) (2011) 1272-1276.
[23] M. Taylor, The space group of MnAl3, Acta Crystallographica 14(1) (1961) 84-84.
[24] K. Hiraga, M. Kaneko, Y. Matsuo, S. Hashimoto, The structure of Al3Mn: Close relationship to decagonal quasicrystais, Philosophical Magazine B 67(2) (1993) 193-205.
[25] P. Nellist, S. Pennycook, The principles and interpretation of annular dark-field Z-contrast imaging, Advances in imaging and electron physics 113 (2000) 147-203.
[26] M. Feuerbacher, H. Klein, K. Urban, Plastic deformation properties of the orthorhombic?'-(Al-Pd-Mn) quasicrystal approximant, Philosophical magazine letters 81(9) (2001) 639-647.
[27] M. Feuerbacher, M. Heggen, Elastic energy of metadislocations in complex metallic alloys, Acta Materialia 60(4) (2012) 1703-1711.
[28] D. Hull, D.J. Bacon, Introduction to dislocations, Elsevier2011.
[29] P. Gallagher, The influence of alloying, temperature, and related effects on the stacking fault energy, Metallurgical Transactions 1(9) (1970) 2429-2461.

[30] Z. Guo, A. Miodownik, N. Saunders, J.-P. Schillé, Influence of stacking-fault energy on high temperature creep of alpha titanium alloys, Scripta materialia 54(12) (2006) 2175-2178.
[31] X. Zhang, B. Grabowski, F. Körmann, A.V. Ruban, Y. Gong, R.C. Reed, T. Hickel, J. Neugebauer, Temperature dependence of the stacking-fault Gibbs energy for Al, Cu, and Ni, Physical Review B 98(22) (2018) 224106.
[32] M. Heggen, M. Feuerbacher, Metadislocation reactions and metadislocation networks in the complex metallic alloy ξ'-Al–Pd–Mn, Materials Science and Engineering: A 400 (2005) 89-92.
[33] M. Heggen, M. Feuerbacher, Metadislocation arrangements in the complex metallic alloy ξ'-Al–Pd–Mn, Philosophical Magazine 86(6-8) (2006) 985-990.